AIP Advances

Tunable degree of polarization in a figure-8 fiber laser

Cite as: AIP Advances **12**, 095120 (2022); https://doi.org/10.1063/5.0102747
Submitted: 20 June 2022 • Accepted: 29 August 2022 • Published Online: 26 September 2022

Banoj Kumar Nayak, Cijy Mathai, Dmitry Panna, et al.

Tunable degree of polarization in a figure-8 fiber laser

Cite as: AIP Advances 12, 095120 (2022); doi: 10.1063/5.0102747
Submitted: 20 June 2022 • Accepted: 29 August 2022 •
Published Online: 26 September 2022

Banoj Kumar Nayak, Cijy Mathai, Dmitry Panna, and Eyal Buks[a]

AFFILIATIONS

Andrew and Erna Viterbi Department of Electrical Engineering, Technion, Haifa 32000, Israel

[a]Author to whom correspondence should be addressed: eyal@ee.technion.ac.il

ABSTRACT

We experimentally study a fiber loop laser in a figure-8 configuration and explore the dependency of the degree of polarization on controlled parameters. To account for the experimental observations, a mapping is derived to evaluate the polarization time evolution. The nonlinearity induced by the Kerr effect and gain saturation gives rise to rich dynamics. We find that the degree of polarization can be increased by tuning the system into a region where the mapping has a locally stable fixed point.

I. INTRODUCTION

Scrambling is commonly employed to lower the degree of polarization (DOP) of optical sources when effects such as polarization hole-burning and polarization mode dispersion are unwanted.[1–3] On the other hand, a high DOP is desired for some applications, including the detection of magneto-optic[4,5] and optomechanical effects.[6]

In this study, we explore the DOP of a fiber loop laser in a figure-8 configuration. Mode locking (ML) in figure-8 lasers (F8Ls) has been studied in Refs. 7–11. The stability of a passively mode-locked F8L was studied in Ref. 12. Various types of vector solitary waves have been demonstrated in optical fibers[13–16] and mode-locked fiber lasers.[17,18] Polarization evolution of vector solitary waves has been investigated in optical fibers[18–20] and fiber lasers.[21–28]

Polarization evolution in optical fibers with spatially varying birefringence has been explored in Ref. 29. Polarization evolution of solitary waves in fiber lasers is complex as optical components, e.g., polarization controllers (PCs), laser gain media, optical couplers (OCs), wavelength filters (WLFs), and multiple cavity round trips, contribute to polarization evolution apart from birefringence and dispersion of optical fibers. Reference 24 has shown that the soliton polarization rotation is periodic where the period can be a multiple of the cavity round trip time in a fiber ring laser. It has been shown that soliton dynamics in a mode-locked fiber laser can produce either multiple fixed polarization states occurring periodically or no fixed polarization state at a fixed location of the laser cavity.[30] This can lead to different DOPs depending on the soliton dynamics. F8L is promising as this fiber laser configuration can give rise to sub-picosecond laser pulses in the ML region.[31,32] However, polarization instability is a challenging issue in mode-locked F8L not based on polarization-maintaining fibers.

In our experiment, we employ the rotating quarter-wave plate method[33] to measure the DOP in both continuous wave (CW) and ML regions. We find that for both cases, the DOP can be tuned.

II. EXPERIMENTAL SETUP

A sketch of the experimental setup is shown in Fig. 1. The F8L consists of two fiber optical loops, which are connected through a 50:50 optical coupler (OC). PCs are integrated into both loops.

The right loop serves as a fiber optical loop mirror (FOLM).[34–36] An erbium doped fiber (EDF) of 3.6 m length is integrated into the FOLM to provide gain in the telecom band. The EDF is pumped using a 980 nm diode laser and a wavelength division multiplexer (WDM). The EDF is connected to a long nonlinear single mode fiber (NSMF) of 50 m length. Band selection is performed using a tunable wavelength filter (WLF) of 0.42 nm width and −3 dB insertion loss. A 99 : 1 OC in the right loop is connected to a photodetector (PD), which is probed using a radio frequency spectrum analyzer (RFSA).

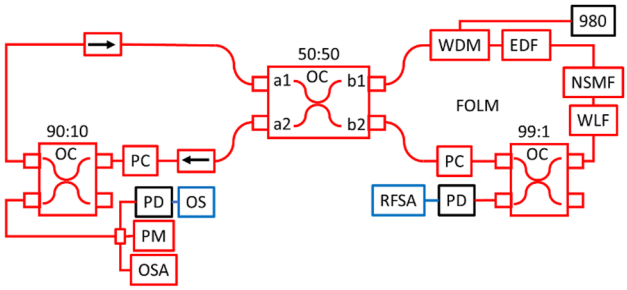

FIG. 1. Figure-8 laser. The FOLM on the right and the unidirectional loop on the left are connected by a 50:50 OC.

For clockwise unidirectional propagation of light in the left loop, two optical isolators (OIs) are employed (labeled by arrows in Fig. 1). A 90:10 OC in the left loop is connected to an optical spectrum analyzer (OSA), a PD, an oscilloscope (OS), and a rotating quarter-wave plate polarimeter (PM) (Thorlabs PA430).

III. MEASUREMENTS

The temporal F8L output signal measured by the OS in the region of ML is shown in Fig. 2(a). Figure 2(b) shows the corresponding autocorrelation (AC) signal as a function of delay time. Figure 2(c) shows the AC signal calculated using Eq. (A4) of Appendix A. The calculated AC signal approximately imitates the coherence artifact (spike) and broad pedestal (wings) of the measured AC. The pulse width is extracted by fitting the data with Eq. (A4) (see caption of Fig. 2).

Plots of the optical spectrum measured using the OSA, the RF spectrum measured using the RFSA, the averaged optical power measured using the PD in the right loop, and the DOP measured using the PM are shown in Fig. 3 as a function of diode current I_D. For the measurements shown in Figs. 3(a1)–3(d1), both PCs are tuned to maximize the DOP in the ML regime, whereas the DOP in the ML regime is minimized for the measurements shown in Figs. 3(a2)–3(d2). For the first (second) case, the CW threshold occurs at a diode current of $I_D = 0.1$ A ($I_D = 0.15$ A), and the ML threshold occurs at $I_D = 0.26$ A ($I_D = 0.37$ A). As can be seen by comparing Figs. 3(d1) and 3(d2), the DOP in the ML regime can be tuned. The DOP plot in Fig. 3(d1) reveals a sharp change in the state of polarization (SOP) at the transition from the CW to the ML regime occurring at a diode current of $I_D = 0.26$ A. For this case, the DOP increases with diode current I_D in both CW and ML regions. An SOP change occurring at the transition from CW to ML regions is also seen in Fig. 3(d2). However, for this case, the DOP remains very low above the transition.

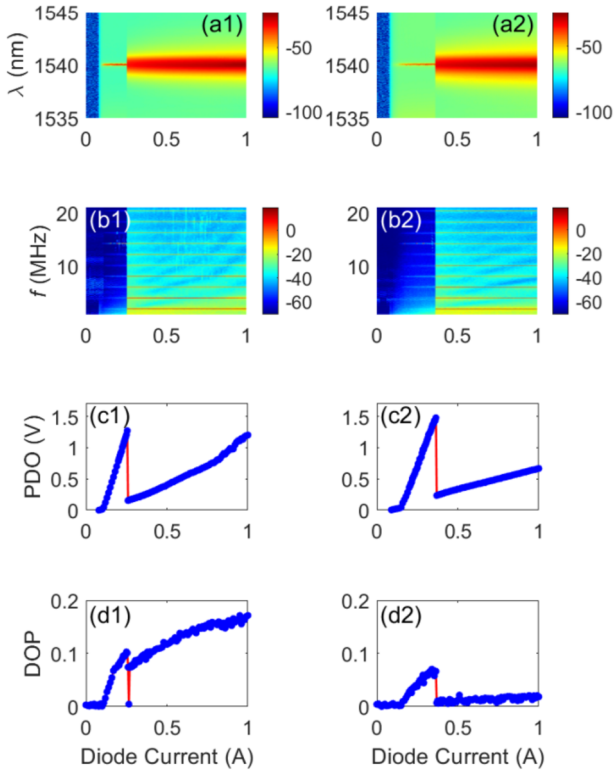

FIG. 3. Dependency on diode current I_D. (a) Optical spectrum (in dBm units) at wavelength λ, (b) RF spectrum (in dBm units) at frequency f, (c) photodetector output power (PDO), and (d) DOP. Left (right) panels, which are labeled "1" ("2"), correspond to the maximized (minimized) DOP in the ML regime. Note that the gain of the PD employed to measure the RF spectrum is set at 10^6 with a bandwidth of 3 MHz. The PD limited bandwidth gives rise to a low pass filtering artifact in the data presented in (b1) and (b2).

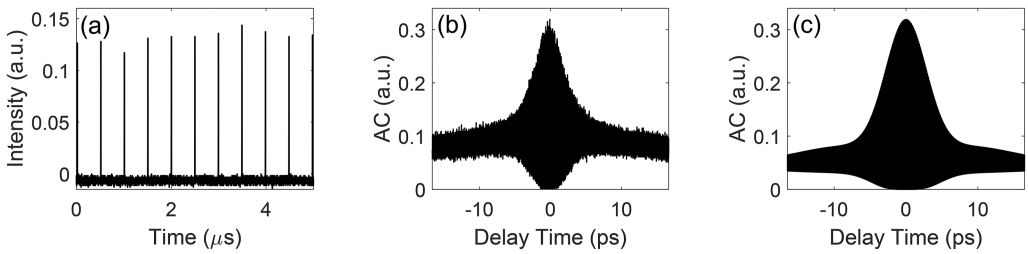

FIG. 2. Mode locking. (a) OS signal as a function of time at diode current $I_D = 1$ A. (b) Measured AC as a function of delay time at diode current $I_D = 1$ A. (c) Calculated AC signal using Eq. (A4) with a pulse width of $\sigma_c = 1.8$ ps and varying splitting time, which follows a normal distribution having a standard deviation of $\sigma_s = 12$ ps.

IV. FOLM

To account for the experimental observations, scattering and birefringence in the FOLM are theoretically studied. The 50:50 OC is characterized by forward (backward) transmission t (t') and reflection r (r') amplitudes. Time reversal and mirror symmetries together with unitarity imply that $t' = t$, $r' = r = it|r/t|$, and $|t|^2 + |r|^2 = 1$.

Consider light having an SOP $|p_{\rm i}\rangle$ being injected into port a1 of the 50:50 OC. The transmitted (reflected) state $|p_{\rm T}\rangle$ ($|p_{\rm R}\rangle$) at port a2 (a1) is given by[37] $|p_{\rm T}\rangle = g\mathcal{A}_{\rm T}|p_{\rm i}\rangle$ ($|p_{\rm R}\rangle = g\mathcal{A}_{\rm R}|p_{\rm i}\rangle$), where the total gain g is real, the operator $\mathcal{A}_{\rm T}$ ($\mathcal{A}_{\rm R}$) is given by $\mathcal{A}_{\rm T} = tt'e^{i\Theta/2}\sigma_z J_+ + rr'e^{-i\Theta/2}J_-\sigma_z$ ($\mathcal{A}_{\rm R} = tr'e^{i\Theta/2}\sigma_z J_+ + rt'e^{-i\Theta/2}J_-\sigma_z$), the nonlinear phase shift Θ is real, $\sigma_z = \mathrm{diag}(1,-1)$ is Pauli's z matrix, and J_+ (J_-) is the Jones matrix corresponding to circulating the FOLM loop in the clockwise (counter clockwise) direction. The assumption is that both J_+ and J_- are unitary, i.e., $J_+^\dagger J_+ = J_-^\dagger J_- = 1$, and together with the relations,

$$\mathcal{A}_{\rm T}^\dagger\mathcal{A}_{\rm T} = \mathcal{J}^\dagger\begin{pmatrix} t^*t'^* \\ r^*r'^* \end{pmatrix}\begin{pmatrix} tt' & rr' \end{pmatrix}\mathcal{J} = \mathcal{J}^\dagger\begin{pmatrix} |t|^2 \\ -|r|^2 \end{pmatrix}\begin{pmatrix} |t|^2 & -|r|^2 \end{pmatrix}\mathcal{J} \tag{1}$$

and

$$\mathcal{A}_{\rm R}^\dagger\mathcal{A}_{\rm R} = \mathcal{J}^\dagger\begin{pmatrix} t^*r'^* \\ r^*t'^* \end{pmatrix}\begin{pmatrix} tr' & rt' \end{pmatrix}\mathcal{J} = |rt|^2\,\mathcal{J}^\dagger\begin{pmatrix} 1 \\ 1 \end{pmatrix}\begin{pmatrix} 1 & 1 \end{pmatrix}\mathcal{J}, \tag{2}$$

where

$$\mathcal{J}^\dagger = \left(e^{-\frac{i\Theta}{2}}J_+^\dagger\sigma_z,\ e^{\frac{i\Theta}{2}}\sigma_z J_-^\dagger\right) \tag{3}$$

yields

$$\mathcal{A}_{\rm T}^\dagger\mathcal{A}_{\rm T} = \left(|t|^2 - |r|^2\right)^2 + 2|rt|^2(1-S), \tag{4}$$

$$\mathcal{A}_{\rm R}^\dagger\mathcal{A}_{\rm R} = 2|rt|^2(1+S), \tag{5}$$

where the operator S is given by (note that $\sigma_z^2 = 1$)

$$S = \frac{e^{-i\Theta}J_+^\dagger\sigma_z J_-\sigma_z + e^{i\Theta}\sigma_z J_-^\dagger\sigma_z J_+}{2}. \tag{6}$$

These relations imply the unitarity condition

$$\mathcal{A}_{\rm T}^\dagger\mathcal{A}_{\rm T} + \mathcal{A}_{\rm R}^\dagger\mathcal{A}_{\rm R} = \left(|t|^2 - |r|^2\right)^2 + 4|rt|^2 = 1. \tag{7}$$

A derivation (see Appendix B) similar to the one that yields the Heisenberg uncertainty principle is employed to derive a lower bound upon the FOLM reflectivity $P_{\rm R} = \langle p|\mathcal{A}_{\rm R}^\dagger\mathcal{A}_{\rm R}|p\rangle/\langle p|p\rangle$ (the commutation relation is denoted by $[\cdot,\cdot]_-$),

$$P_{\rm R} \geq \frac{|rt|^2\left|\mathrm{Re}\langle p|e^{-i\Theta}\left[J_+^\dagger\sigma_z, J_-\sigma_z\right]_-|p\rangle\right|}{\langle p|p\rangle}. \tag{8}$$

The relation $\mathcal{A}_{\rm T}^\dagger\mathcal{A}_{\rm T} + \mathcal{A}_{\rm R}^\dagger\mathcal{A}_{\rm R} = 1$ together with inequality (8) yields an upper bound upon the FOLM transmissivity $P_{\rm T} = \langle p|\mathcal{A}_{\rm T}^\dagger\mathcal{A}_{\rm T}|p\rangle/\langle p|p\rangle$. However, both $P_{\rm R}$ and $P_{\rm T}$ become unbounded when $\left[J_+^\dagger\sigma_z, J_-\sigma_z\right]_- = 0$. In particular, no bound is imposed by inequality (8) when $J_- = \sigma_z J_+\sigma_z$. As will be shown below, the condition $J_- = \sigma_z J_+\sigma_z$ is satisfied when the SOP evolution along the FOLM depends only on the geometry of the fiber spatial curve.

V. SOP EVOLUTION

The Jones matrices J_+ and J_- can be calculated by integrating the equation of motion for the SOP along the FOLM. Consider an optical fiber winded in some spatial curve in space. Let $\mathbf{r}(s)$ be the arc-length parametrization of this curve, i.e., the tangent $\hat{\mathbf{s}} = \mathrm{d}\mathbf{r}/\mathrm{d}s$ is a unit vector. The normal and binormal Serret–Frenet unit vectors are denoted by $\hat{\boldsymbol{\nu}}$ and $\hat{\mathbf{b}}$, respectively. The curve torsion τ is defined as $\mathrm{d}\hat{\mathbf{b}}/\mathrm{d}s = -\tau\hat{\boldsymbol{\nu}}$.[38] A unit vector parallel to the electric field is denoted by $\hat{\mathbf{e}}_0$. In the Serret–Frenet frame, the unit vector $\hat{\mathbf{e}}_0$, which is expressed as $\hat{\mathbf{e}}_0 = e_\nu\hat{\boldsymbol{\nu}} + e_b\hat{\mathbf{b}}$, evolves according to the parallel transport equation of geometrical optics as[39–41]

$$\frac{\mathrm{d}}{\mathrm{d}s}\begin{pmatrix} e_\nu \\ e_b \end{pmatrix} = i\mathcal{K}\begin{pmatrix} e_\nu \\ e_b \end{pmatrix}, \tag{9}$$

where $\mathcal{K} = \mathcal{K}_{\rm g} + \mathcal{K}_{\rm f}$. The geometrical birefringence $\mathcal{K}_g$ is given by[40,42]

$$\mathcal{K}_{\rm g} = \tau\begin{pmatrix} 0 & -i \\ i & 0 \end{pmatrix}, \tag{10}$$

whereas $\mathcal{K}_{\rm f}$ is the fiber birefringence induced by elasto-optic, electro-optic, or magneto-optic effects. For a lossless fiber, the matrix $\mathcal{K}$ is Hermitian.

Consider the case where $\mathcal{K}_{\rm f}$ vanishes. For this case, the solution to Eq. (9) is given by[38]

$$\begin{pmatrix} e_\nu(s) \\ e_b(s) \end{pmatrix} = \begin{pmatrix} \cos\theta & \sin\theta \\ -\sin\theta & \cos\theta \end{pmatrix}\begin{pmatrix} e_\nu(0) \\ e_b(0) \end{pmatrix}, \tag{11}$$

where the rotation angle θ is given by the integrated torsion along the fiber curve,

$$\theta = \int_0^s \mathrm{d}s'\tau(s'). \tag{12}$$

For the case where the curve end points are parallel, i.e., $\hat{\mathbf{s}}(s) = \hat{\mathbf{s}}(0)$, the following holds good: $\theta = \Omega$, where Ω is the solid angle subtended by the closed curve $\hat{\mathbf{s}}(s')$ at the origin. This geometrical rotation of polarization, which is closely related to Berry's phase,[43] has been experimentally measured in Refs. 42 and 44.

For the case $\mathcal{K}_f = 0$, $J_- = \sigma_z J_+ \sigma_z$ holds good, and consequently, $S = \cos\Theta$, $\mathcal{A}_T^\dagger \mathcal{A}_T = \left(|t|^2 - |r|^2\right)^2 + 4|rt|^2 \sin^2(\Theta/2)$, and $\mathcal{A}_R^\dagger \mathcal{A}_R = 4|rt|^2 \cos^2(\Theta/2)$ (it is assumed that $J_+^\dagger J_+ = 1$). Hence, for this case, both reflectivity P_R and transmissivity P_T become independent of the input SOP. For a 3 dB OC, i.e., $|t|^2 = |r|^2 = 1/2$, and in the linear limit, i.e., for $\Theta = 0$, the FOLM for the same case where $\mathcal{K}_f = 0$ becomes perfectly reflecting, i.e., $P_T = 0$ and $P_R = 1$.

For treating the general case (where $\mathcal{K}_f$ cannot be disregarded and consequently FOLM's perfect reflectivity cannot be guaranteed), it is convenient to express the matrix J_- as $J_- = J_m \sigma_z J_+ \sigma_z$, where J_m is unitary, i.e., $J_m^\dagger J_m = 1$. Using this notation, one finds that

$$P_R = 4|rt|^2(1-\eta)\,, \tag{13}$$

$$P_T = \left(|t|^2 - |r|^2\right)^2 + 4|rt|^2\,\eta\,, \tag{14}$$

where

$$\eta = \sin^2\frac{\Theta}{2} - \frac{\mathrm{Re}\left(e^{-i\Theta}\langle p|J_+^\dagger V_m J_+|p\rangle\right)}{2\langle p|p\rangle} \tag{15}$$

and $V_m = \sigma_z(J_m - 1)\sigma_z$. Note that $J_m = 1$ and $V_m = 0$ for the case $\mathcal{K}_f = 0$.

VI. MAPPING

In this section, a cycle to cycle mapping is derived to analyze the SOP evolution. Stability analysis of the mapping allows DOP evaluation in the steady state. The input SOP $|p_i\rangle$ after n cycles is denoted by $|p_n\rangle$. The mapping between $|p_n\rangle$ and $|p_{n+1}\rangle$ is given by

$$|p_{n+1}\rangle = g J_L \mathcal{A}_T |p_n\rangle, \tag{16}$$

where the Jones matrix of the clockwise unidirectional left loop, which is denoted by J_L, is assumed to be unitary, i.e., $J_L^\dagger J_L = 1$. The mapping equation (16) is nonlinear since $\mathcal{A}_T$ depends on the nonlinear phase Θ, which, in turn, depends on the intensity $I_n = \langle p_n|p_n\rangle$. In addition, the gain g may vary due to saturation. In general, the nonlinear phase Θ may also depend on the SOP; however, this dependency is expected to be relatively weak since our setup is based on regular (rather than polarization maintaining) single mode fibers. The amplification factor I_{n+1}/I_n corresponding to the SOP $|p_n\rangle$ is denoted by $\mathcal{F}(|p_n\rangle)$, where $\mathcal{F}(|p\rangle) = g^2\langle p|\mathcal{A}_T^\dagger \mathcal{A}_T|p\rangle/\langle p|p\rangle$.

The blue lines in Fig. 4 represent the values of $|\lambda_1|$ and $|\lambda_2|$ as a function of Θ for four different cases, where $\lambda_{1,2}$ are the eigenvalues of $J_L\mathcal{A}_T$. The unitary matrices J_+, J_m, and J_L are expressed as $J_+ = U(\theta_+, \varphi_+, \phi_+)$, $J_m = U(\theta_m, \varphi_m, \phi_m)$, and $J_L = U(\theta_L, \varphi_L, \phi_L)$, respectively, where

$$U(\theta,\varphi,\phi) = \begin{pmatrix} \cos\frac{\phi}{2} - i\cos\theta\sin\frac{\phi}{2} & -i\sin\theta e^{-i\varphi}\sin\frac{\phi}{2} \\ -i\sin\theta e^{i\varphi}\sin\frac{\phi}{2} & \cos\frac{\phi}{2} + i\cos\theta\sin\frac{\phi}{2} \end{pmatrix}, \tag{17}$$

and where all angles θ, φ, and ϕ are real. The matrix $U(\theta,\varphi,\phi)$ represents the SOP rotation around the unit vector $(\sin\theta\cos\varphi, \sin\theta\sin\varphi, \cos\theta)$ by an angle ϕ. The red lines in Fig. 4 represent the values of $\Lambda_1^{1/2}$ and $\Lambda_2^{1/2}$, where $\Lambda_{1,2}$ are the non-negative eigenvalues of the Hermitian and positive-definite operator

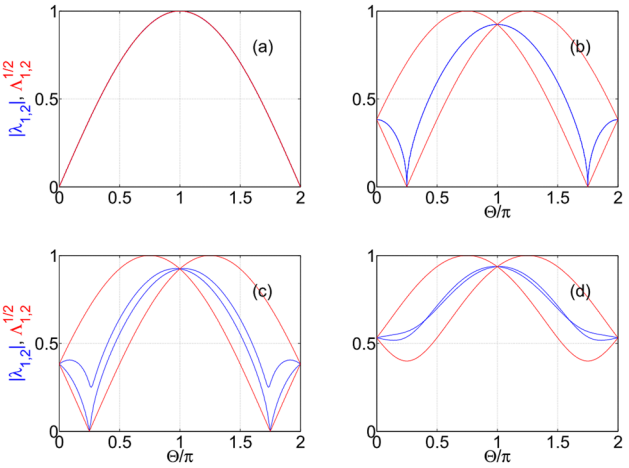

FIG. 4. Eigenvalues of $J_L\mathcal{A}_T$ (blue) and $\mathcal{A}_T^\dagger\mathcal{A}_T$ (red) as a function of the nonlinear phase Θ. (a) The following values are assumed for the calculation: $\theta_+ = 0$, $\varphi_+ = 0$, $\phi_+ = 0$, $\theta_m = 0.5\pi$, $\varphi_m = 0$, $\phi_m = 0$, $\theta_L = 0$, $\varphi_L = 0$, $\phi_L = 0$, and $t = (1/2)^{1/2}$. In the description given below for the other panels, only modified (with respect to previous panels) parameters are specified. (b) $\phi_m = -0.5\pi$. (c) $\theta_L = 0.25\pi$, $\varphi_L = 0.5\pi$, and $\phi_L = 0.25\pi$. (d) $t = (0.3)^{1/2}$.

$\mathcal{A}_T^\dagger\mathcal{A}_T$. Let $|p_F\rangle$ be an SOP, for which the amplification factor $\mathcal{F}(|p\rangle)$ is maximized (for a given Θ). If, in addition, $|p_F\rangle$ is an eigenvector of the mapping operator $gJ_L\mathcal{A}_T$, then the DOP is expected to be relatively high in the steady state, provided that $|p_F\rangle$ is a locally stable fixed point of the mapping Eq. (16). For the case shown in Fig. 4(a), for which the operator $\mathcal{A}_T$ is given by $\mathcal{A}_T = i\sin(\Theta/2)\sigma_z$, the SOP $|p_F\rangle$ is an eigenvector of $gJ_L\mathcal{A}_T$ for all Θ [note that $|\lambda_{1,2}| = \Lambda_{1,2}^{1/2} = \sin(\Theta/2)$ for this case]. The equality $|\lambda_{1,2}| = \Lambda_{1,2}^{1/2}$ [see Fig. 4(a)] is violated by the transformation J_m [see Fig. 4(b)], and the equality $|\lambda_1| = |\lambda_2|$ [see Figs. 4(a) and 4(b)] is violated by the transformation J_L [see Fig. 4(c)]. The effect of violating the condition $|t|^2 = |r|^2$ is demonstrated in Fig. 4(d).

The drop in PDO [see Figs. 3(c1) and 3(c2)] and the DOP [see Figs. 3(d1) and 3(d2)] occurring in the transition from CW to ML is attributed to the change in peak power, which, in turn, affects SOP evolution due to nonlinearity of the cycle to cycle mapping equation (16) (induced by both Kerr effect and gain saturation). The drop in PDO represents the change in the averaged optical loss per cycle, which depends on the FOLM reflectivity P_R. A bifurcation diagram example of the mapping Eq. (16) is shown in Fig. 5. The parameters that are used for the calculation are listed in the figure caption. To account for saturation, the gain g is assumed to be given by

$$g = \frac{g_0}{1 + \frac{I}{I_s}}, \tag{18}$$

where g_0 is the small signal gain and I_s is the saturation intensity. The Kerr effect induced nonlinear phase Θ is assumed to be given by $\Theta = \zeta I$, where ζ is a positive constant and where $I = \langle p|p\rangle$ is the intensity. For the example shown in Fig. 5, a period doubling bifurcation occurs at $g_0 = 4.18$. A relatively low DOP is expected in

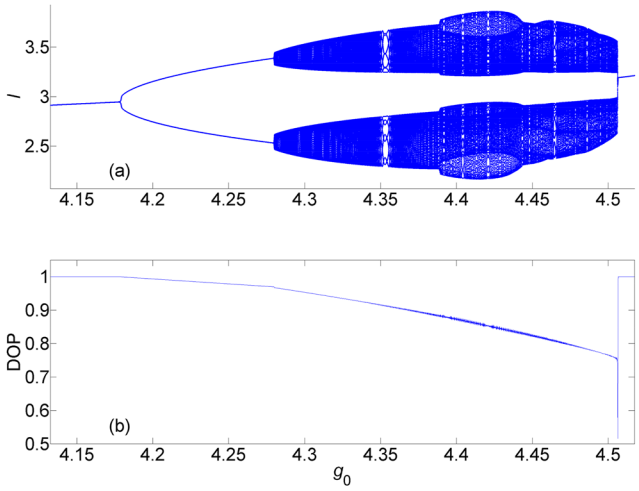

FIG. 5. A bifurcation diagram. The (a) intensity I and (b) DOP plotted as a function of the small signal gain g_0. The parameters assumed for the calculations are $\phi_+ = 0$, $\theta_m = 0.5\pi$, $\varphi_m = 0$, $\phi_m = -0.5\pi$, $\theta_L = 0.5\pi$, $\varphi_L = 0.5\pi$, $\phi_L = 0.5\pi$, $t = (1/2)^{1/2}$, $\zeta = 1$, and $I_s = 1$.

the region $4.28 \le g_0 \le 4.51$, where the period time of the mapping equation (16) becomes much longer than the loop fundamental period.

Note that the mapping equation (16) strongly depends on the unitary matrices J_+, J_m, and J_L. In the experiment, this dependency can be explored by tuning both PCs. The dependency shown in Fig. 3, of both PDO and DOP on diode current I_D, can be significantly modified by retuning both PCs. Similarly, the bifurcation diagram shown in Fig. 5 can be significantly modified by changing the assumed unitary matrices. In a fiber-based setup, it is very difficult to independently measure each of these unitary matrices for any given paddle configuration of both PCs. However, when these unitary matrices are treated as fitting parameters, good agreement between theory and experiment can be obtained.

VII. SUMMARY

In summary, DOP tunability is experimentally demonstrated in an F8L, in both CW and ML regions. The mapping equation (16) is employed to derive the SOP time evolution. A high DOP can be obtained in the regions where the mapping has a locally stable fixed point. The nonlinearity of the cycle to cycle SOP mapping equation (16) gives rise to complex dynamics. The current experimental setup, which is based on the rotating quarter-wave plate method, does not allow monitoring of the relatively fast SOP cycle to cycle evolution since the fiber ring period time is much shorter than the plate rotation period time. Future experiments, which will employ a faster polarimeter, will be devoted to the cycle to cycle complex dynamics of this system.

ACKNOWLEDGMENTS

We thank A. Becker and V. Smulkovsky for technical help. This work was supported by the Israeli Science Foundation, the Israeli Ministry of Science, and by the Technion Security Research Foundation.

AUTHOR DECLARATIONS

Conflict of Interest

The authors have no conflicts to disclose.

Author Contributions

Banoj Kumar Nayak: Investigation (lead); Methodology (equal); Data curation (lead); Writing – original draft (lead). **Cijy Mathai**: Methodology (equal). **Dmitry Panna**: Methodology (equal). **Eyal Buks**: Supervision (lead); Formal analysis (lead); Writing – original draft (lead).

DATA AVAILABILITY

The data that support the findings of this study are available from the corresponding author upon reasonable request.

APPENDIX A: AUTOCORRELATION

In a Michelson interferometer with a second harmonic signal, the detector signal $I_C(\tau)$ corresponding to second-order interferometric correlation can be written as a function of delay time τ as [see Eq. (9.6) of Ref. 45] as

$$I_C(\tau, E(t)) = \int_{-\infty}^{\infty} dt \left|(E(t) + E(t-\tau))^2\right|^2 , \tag{A1}$$

where $E(t) = e^{i\omega_0 t} f_{\sigma_c}^{1/2}(t)$ is the electric field of a Gaussian partial pulse at time t [see Eq. (2.39) of Ref. 46], ω_0 is the carrier angular frequency, and the normal distribution function having a standard deviation σ and a vanishing expectation value is given by

$$f_\sigma(x) = \frac{1}{\sigma\sqrt{2\pi}} \exp\left(-\frac{x^2}{2\sigma^2}\right). \tag{A2}$$

The pulse full width at half maxima is $2\sqrt{2}\left(\ln^{1/2} 2\right)\sigma_c$.

A fitting based on Eq. (A1) could not accurately replicate the broad pedestal (wings) in our experimental AC data shown in Fig. 2(b). Better agreement can be obtained from a double-pulse model, which assumes pulse splitting with a varying separation time t_s (see Fig. 4.8 of Ref. 46). The splitting gives rise to the so-called coherence artifact. In this model, the electric field $E_s(t, t_s)$ is assumed to be given by

$$E_s(t, t_s) = e^{i\omega_0 t} \frac{f_{\sigma_c}^{1/2}\left(t - \frac{t_s}{2}\right) + f_{\sigma_c}^{1/2}\left(t + \frac{t_s}{2}\right)}{2} . \tag{A3}$$

The double-pulse assumption is supported by Ref. 47, which demonstrates transition from the single-pulsing to the double-pulsing regime with increasing pump current beyond the single-pulsing instability threshold. In our case, the time of separation t_s is

considered to have a normal distribution with standard deviation σ_s. The averaged AC signal, which is denoted by $\langle I_C(\tau)\rangle$, is given by

$$\langle I_C(\tau)\rangle = \int_{-\infty}^{\infty} dt_s\, f_{\sigma_s}(t_s) I_C(\tau, E_s(t,t_s))\,. \tag{A4}$$

The values of both standard deviations σ_c and σ_s are extracted by data fitting (see the caption of Fig. 2).

APPENDIX B: INEQUALITY (8)

The positive definite operator $\mathcal{A}_R^\dagger \mathcal{A}_R$ can be expressed as

$$\mathcal{A}_R^\dagger \mathcal{A}_R = \frac{\left[\mathcal{A}_R^\dagger, \mathcal{A}_R\right] + \left[\mathcal{A}_R^\dagger, \mathcal{A}_R\right]_+}{2}, \tag{B1}$$

where $\left[\mathcal{A}_R^\dagger, \mathcal{A}_R\right]_- = \mathcal{A}_R^\dagger \mathcal{A}_R - \mathcal{A}_R^\dagger \mathcal{A}_R$ is anti-Hermitian and $\left[\mathcal{A}_R^\dagger, \mathcal{A}_R\right]_+ = \mathcal{A}_R^\dagger \mathcal{A}_R + \mathcal{A}_R \mathcal{A}_R^\dagger$ is Hermitian; thus,

$$\left|\frac{\langle p|\mathcal{A}_R^\dagger \mathcal{A}_R|p\rangle}{\langle p|p\rangle}\right|^2 \geq \left|\frac{\langle p|\left[\mathcal{A}_R^\dagger, \mathcal{A}_R\right]_-|p\rangle}{2\langle p|p\rangle}\right|^2. \tag{B2}$$

The relation $\mathcal{A}_R = tr' e^{i\Theta/2}\sigma_z J_+ + rt' e^{-i\Theta/2} J_- \sigma_z$ yields (recall that it is assumed that $J_+^\dagger J_+ = J_-^\dagger J_- = 1$)

$$\frac{\left[\mathcal{A}_R^\dagger, \mathcal{A}_R\right]_-}{|rt|^2} = e^{-i\Theta}\langle p|\left[J_+^\dagger \sigma_z, J_- \sigma_z\right]_-|p\rangle + e^{i\Theta}\langle p|\left[\sigma_z J_-^\dagger, \sigma_z J_+\right]_-|p\rangle; \tag{B3}$$

hence,

$$\frac{\left|\frac{\langle p|\mathcal{A}_R^\dagger \mathcal{A}_R|p\rangle}{\langle p|p\rangle}\right|^2}{|rt|^4} \geq \left|\frac{\mathrm{Re}\left(e^{-i\Theta}\langle p|\left[J_+^\dagger \sigma_z, J_- \sigma_z\right]_-|p\rangle\right)}{\langle p|p\rangle}\right|^2, \tag{B4}$$

and, thus, the inequality equation (8) holds good.

REFERENCES

[1] J. C. Cheng, L. A. Nafie, and P. J. Stephens, "Polarization scrambling using a photoelastic modulator: Application to circular dichroism measurement," J. Opt. Soc. Am. **65**(9), 1031–1035 (1975).

[2] M. Safari and A. A. Shishegar, "Analysis of degree of polarization as a control signal in PMD compensation systems aided by polarization scrambling," J. Lightwave Technol. **26**(16), 2865–2872 (2008).

[3] J. F. Barrera, A. Vélez, and R. Torroba, "Experimental scrambling and noise reduction applied to the optical encryption of QR codes," Opt. Express **22**(17), 20268–20277 (2014).

[4] R. Duggan, D. Sounas, and A. Alu, "Optically driven effective Faraday effect in instantaneous nonlinear media," Optica **6**(9), 1152–1157 (2019).

[5] S. Ali, J. R. Davies, and J. T. Mendonca, "Inverse Faraday effect with linearly polarized laser pulses," Phys. Rev. Lett. **105**(3), 035001 (2010).

[6] L. He, H. Li, and M. Li, "Optomechanical measurement of photon spin angular momentum and optical torque in integrated photonic devices," Sci. Adv. **2**(9), e1600485 (2016).

[7] I. N. Duling, "All-fiber ring soliton laser mode locked with a nonlinear mirror," Opt. Lett. **16**(8), 539–541 (1991).

[8] H. Lin, D. K. Donald, and W. V. Sorin, "Optimizing polarization states in a figure-8 laser using a nonreciprocal phase shifter," J. Lightwave Technol. **12**(7), 1121–1128 (1994).

[9] R. Liao, Y. Song, L. Chai, and M. Hu, "Pulse dynamics manipulation by the phase bias in a nonlinear fiber amplifying loop mirror," Opt. Express **27**(10), 14705–14715 (2019).

[10] N. Kuse, J. Jiang, C.-C. Lee, T. R. Schibli, and M. E. Fermann, "All polarization-maintaining Er fiber-based optical frequency combs with nonlinear amplifying loop mirror," Opt. Express **24**(3), 3095–3102 (2016).

[11] W. Hänsel, H. Hoogland, M. Giunta, S. Schmid, T. Steinmetz, R. Doubek, P. Mayer, S. Dobner, C. Cleff, M. Fischer, and R. Holzwarth, "All polarization-maintaining fiber laser architecture for robust femtosecond pulse generation," in *Exploring the World with the Laser* (Springer, 2018), pp. 331–340.

[12] M. Salhi, A. Haboucha, H. Leblond, and F. Sanchez, "Theoretical study of figure-eight all-fiber laser," Phys. Rev. A **77**(3), 033828 (2008).

[13] C. R. Menyuk, "Stability of solitons in birefringent optical fibers. I: Equal propagation amplitudes," Opt. Lett. **12**(8), 614–616 (1987).

[14] C. R. Menyuk, "Stability of solitons in birefringent optical fibers. II. Arbitrary amplitudes," J. Opt. Soc. Am. B **5**(2), 392–402 (1988).

[15] V. V. Afanasjev, "Soliton polarization rotation in fiber lasers," Opt. Lett. **20**(3), 270–272 (1995).

[16] D. N. Christodoulides and R. I. Joseph, "Vector solitons in birefringent nonlinear dispersive media," Opt. Lett. **13**(1), 53–55 (1988).

[17] N. N. Akhmediev, J. M. Soto-Crespo, S. T. Cundiff, B. C. Collings, and W. H. Knox, "Phase locking and periodic evolution of solitons in passively mode-locked fiber lasers with a semiconductor saturable absorber," Opt. Lett. **23**(11), 852–854 (1998).

[18] S. T. Cundiff, B. C. Collings, N. N. Akhmediev, J. M. Soto-Crespo, K. Bergman, and W. H. Knox, "Observation of polarization-locked vector solitons in an optical fiber," Phys. Rev. Lett. **82**(20), 3988 (1999).

[19] Y. Silberberg and Y. Barad, "Rotating vector solitary waves in isotropic fibers," Opt. Lett. **20**(3), 246–248 (1995).

[20] Y. Barad and Y. Silberberg, "Polarization evolution and polarization instability of solitons in a birefringent optical fiber," Phys. Rev. Lett. **78**(17), 3290 (1997).

[21] S. V. Sergeyev, C. Mou, E. G. Turitsyna, A. Rozhin, S. K. Turitsyn, and K. Blow, "Spiral attractor created by vector solitons," Light: Sci. Appl. **3**(1), e131 (2014).

[22] B. C. Collings, S. T. Cundiff, N. N. Akhmediev, J. M. Soto-Crespo, K. Bergman, and W. H. Knox, "Polarization-locked temporal vector solitons in a fiber laser: Experiment," J. Opt. Soc. Am. B **17**(3), 354–365 (2000).

[23] H. Zhang, D. Y. Tang, L. M. Zhao, and H. Y. Tam, "Induced solitons formed by cross-polarization coupling in a birefringent cavity fiber laser," Opt. Lett. **33**(20), 2317–2319 (2008).

[24] L. M. Zhao, D. Y. Tang, H. Zhang, and X. Wu, "Polarization rotation locking of vector solitons in a fiber ring laser," Opt. Express **16**(14), 10053–10058 (2008).

[25] H. Zhang, D. Y. Tang, L. M. Zhao, and X. Wu, "Observation of polarization domain wall solitons in weakly birefringent cavity fiber lasers," Phys. Rev. B **80**(5), 052302 (2009).

[26] D. Y. Tang, H. Zhang, L. M. Zhao, and X. Wu, "Observation of high-order polarization-locked vector solitons in a fiber laser," Phys. Rev. Lett. **101**(15), 153904 (2008).

[27] C. Mou, S. Sergeyev, A. Rozhin, and S. Turistyn, "All-fiber polarization locked vector soliton laser using carbon nanotubes," Opt. Lett. **36**(19), 3831–3833 (2011).

[28] L. J. Wang, J. T. Lin, and P. Ye, "Analysis of polarization-dependent gain in fiber amplifiers," IEEE J. Quantum Electron. **34**(3), 413–418 (1998).

[29] C. R. Menyuk and P. K. A. Wai, "Polarization evolution and dispersion in fibers with spatially varying birefringence," J. Opt. Soc. Am. B **11**(7), 1288–1296 (1994).

[30] J. Wu, D. Y. Tang, L. M. Zhao, and C. C. Chan, "Soliton polarization dynamics in fiber lasers passively mode-locked by the nonlinear polarization rotation technique," Phys. Rev. E **74**(4), 046605 (2006).

[31] W. Wang, F. Wang, Y. Zhang, H. Ma, Q. Yu, and X. Zhang, "Passively mode-locked figure-eight fiber laser using a compact power-imbalanced nonlinear optical-loop mirror," J. Russ. Laser Res. **37**(3), 265–272 (2016).

[32] J. Peng, L. Zhan, Z. Gu, K. Qian, S. Luo, and Q. Shen, "Direct generation of 128-fs Gaussian pulses from a compensation-free fiber laser using dual mode-locking mechanisms," Opt. Commun. **285**(5), 731–733 (2012).

[33] D. H. Goldstein, *Polarized Light* (CRC Press, 2017).

[34]N. J. Doran and D. Wood, "Nonlinear-optical loop mirror," Opt. Lett. **13**(1), 56–58 (1988).
[35]D. B. Mortimore, "Fiber loop reflectors," J. Lightwave Technol. **6**(7), 1217–1224 (1988).
[36]B. Ibarra-Escamilla, E. A. Kuzin, O. Pottiez, J. W. Haus, F. Gutierrez-Zainos, R. Grajales-Coutiño, and P. Zaca-Moran, "Fiber optical loop mirror with a symmetrical coupler and a quarter-wave retarder plate in the loop," Opt. Commun. **242**(1–3), 191–197 (2004).
[37]E. Buks and B. Kumar Nayak, "Quantum measurement with recycled photons," Phys. Rev. B **105**(1), 014421 (2022).
[38]E. Buks, "Adiabatic breakdown in a fiber ring resonator," J. Opt. Soc. Am. B **23**, 628–636 (2006).
[39]S. M. Rytov, Dokl. Akad. Nauk SSSR **18**, 263 (1938).
[40]S. Pancharatnam, "Generalized theory of interference and its applications," Proc. Indian Acad. Sci., Sec. A **44**, 398–417 (1956).
[41]Y. A. Kravtsov and Y. I. Orlov, *Geometrical Optics of Inhomogeneous Media* (Springer, 1990), Vol. 38.
[42]J. N. Ross, "The rotation of the polarization in low birefringence monomode optical fibres due to geometric effects," Opt. Quantum Electron. **16**(5), 455–461 (1984).
[43]M. V. Berry, "Quantal phase factors accompanying adiabatic changes," Proc. R. Soc. London, Ser. A **392**(1802), 45–57 (1984).
[44]A. Tomita and R. Y. Chiao, "Observation of Berry's topological phase by use of an optical fiber," Phys. Rev. Lett. **57**(8), 937 (1986).
[45]J.-C. Diels and W. Rudolph, *Ultrashort Laser Pulse Phenomena* (Elsevier, 2006).
[46]R. Trebino, *Frequency-Resolved Optical Gating: The Measurement of Ultrashort Laser Pulses* (Springer Science & Business Media, 2000).
[47]B. G. Bale, K. Kieu, J. N. Kutz, and F. Wise, "Transition dynamics for multi-pulsing in mode-locked lasers," Opt. Express **17**(25), 23137–23146 (2009).